Journal of Materials Chemistry A

Accepted Manuscript

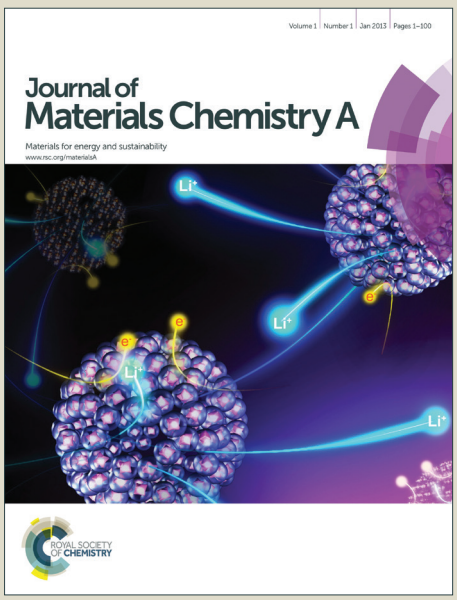

ROYAL SOCIETY OF CHEMISTRY

www.rsc.org/materialsA

Nanometer scale interface engineering boosts the thermoelectric performance of n-type $Ti_{0.4}Hf_{0.6}Ni_{1+z}Sn_{0.975}Sb_{0.025}$ alloys

Pranati Sahoo, Yuanfeng Liu and Pierre F. P. Poudeu*

Laboratory for Emerging Energy and Electronic Materials, Department of Materials Science and Engineering , University of Michigan, Ann Arbor, MI 48109, USA

KEYWORDS: Nanostructuring · Mechanical Alloying · Half-Heusler/Full-Heusler ·Thermoelectric properties · Thermal Conductivity ·

*Corresponding author. Tel: +1-734-763-8436; Fax: +1-734-763-4788

E-mail address: ppoudeup@umich.edu

RECEIVED DATE……

Abstract

Engineering the internal structure of bulk semiconductors through the introduction of nanometer scale interfaces affords opportunities for simultaneous optimization of electronic and thermal transport properties; enabling the fabrication of nanocomposite materials with superior thermoelectric performance. Several compositions of n-type $Ti_{0.4}Hf_{0.6}Ni_{1+z}Sb_{0.975}Sn_{0.025}$ half-Heusler(HH)/full-Heusler(FH) composites were synthesized using high temperature solid state reaction of the elements. Polycrystalline powders of the resulting HH(1-z)/FH(z) composites were further processed by mechanical alloying using high-energy ball milling. Transmission electron microscopy (TEM) studies revealed the presence of small (~20 nm) FH precipitates coherently embedded in micron scale grains of HH/FH composites obtained after solid state reaction, whereas nanometer scale grains (~20 nm) of the HH/FH composites containing very small (< 10 nm) FH precipitates were observed in mechanical alloyed samples (SS-MA). The as-synthesized HH(1-z)/FH(z) samples (SS) showed similar electrical conductivity, thermopower and thermal conductivity at all temperatures regardless of the fractions of FH inclusions. This suggests that the FH inclusions are electronically inert with regards to the matrix. Interestingly, drastic alterations of all three properties were observed on mechanically alloyed samples and the magnitude of change in various properties increase with the mole fractions of FH inclusions. For example, large reductions in the thermal conductivity (8.5 W/ Km to 4.0 W/Km at 300K) as well as electrical conductivity (4750 S/cm to 1750 S/cm at 300K) were observed on all SS-MA samples compared to SS samples with similar compositions. This behavior is attributed to enhanced scattering of phonons and electrons at multiple grain boundaries generated by the mechanical alloying process. Remarkably, the magnitude of the reduction in the electrical and thermal conductivities increases with the mole fraction of FH inclusions in the samples suggesting (1) reduction in carrier density due to trapping of low-energy carriers and (2) additional phonon scattering at nanometer scale HH/FH interfaces. This results in large increases in the thermopower (-60 μV/K to -92 μV/K at 300K) of SS-MA samples, which mitigates the drop in the electrical conductivity leading to large improvement of the figure of merit of mechanically alloyed $Ti_{0.4}Hf_{0.6}Ni_{1+z}Sb_{0.975}Sn_{0.025}$ samples.

Introduction

Bulk nanostructured semiconductors have attracted considerable attention over the past two decades due to their superior thermoelectric properties when compared to nanostructure-free counterparts[1-6]. Several studies have shown that the thermoelectric figure of merit, ZT, of a bulk semiconductor can be drastically improved by addition of suitable low-dimensional second phases within its matrix[7-8]. ZT enhancements in such nanostructured semiconductors mainly come from a large decrease in the thermal conductivity due to enhanced phonon scattering at matrix/nanostructure interfaces and at the grains boundaries[9-11]. However, ZT enhancements in nanostructured semiconductors due to improvement in the power factor have also been reported[12-14]. Power factor enhancements in these nanostructured materials generally originate from large enhancement in the thermopower achieved by (1) manipulating the electron density of states (DOS) via quantum confinement[12, 15-19] or (2) filtering of low energy carriers at matrix/inclusion interfaces [20-22].

Our previous work on nanostructured half-Heusler (HH) alloys showed that coherently embedded full-Heusler (FH) nanostructures played a vital role in tuning the thermoelectric properties of the HH matrix [23-26]. One approach to *in-situ* growth of nanostructures into bulk HH matrices is the solid state reaction of elements at high temperatures. Bulk nanostructured HH alloys obtained by this method tend to exhibit significantly enhanced thermoelectric properties as compared to samples produced by melting-quenching[27-28] or microwave[29] processes. The long annealing at reasonably high temperature allow for the formation of well crystallized bulk HH and nanometer-scale FH phases. However, in the solid-state method, reaction between the elements is limited by the complexity of solid-state diffusion of reactants, mismatch in reactant/product geometry, phase immiscibility and multiple products obtained at individual stages.[30-31] Therefore, compositionally inhomogeneous products of randomly distributed nanoinclusions, with various sizes, are generally obtained [23-25, 32]. To facilitate a complete reaction of the elements to the desired two-component mixture of HH matrix and FH inclusions and also to improve the distribution of the FH phases, polycrystalline powders from the solid state reactions are further processed by mechanical alloying (MA) using high-energy shaker ball mill. The MA process not only promotes the solid state reaction of the reactants, but also enables the reduction of the average grain size of the HH/FH nanocomposites leading to the formation of a high density of grain boundaries and matrix/inclusion phase boundaries. Here, we investigate

the contribution of these interfaces to the thermoelectric properties of HH(1-z)/FH(z) nanocomposites. We report a comparative study of the internal structure and thermoelectric behavior of n–type $Ti_{0.4}Hf_{0.6}Ni_{1+z}Sb_{0.975}Sn_{0.025}$ **(**HH(1-z)/FH(z)) bulk nanocomposites obtained by (1) solid-state reaction of the elements (SS) and (2) solid state reaction followed by mechanical alloying using high-energy shaker mill (SS-MA). Both series of samples were consolidated under similar conditions (temperature and pressure) using a uniaxial hot press system. Transmission electron microscopy studies revealed the presence of nanometer-scale FH precipitates in both SS and SS-MA series of samples. However, the SS-MA samples showed nanometer scale grains (~20 nm) of the HH/FH composites whereas micron scale grains are observed in the SS samples. This indicates the effectiveness of the MA process in reducing the average grain size of bulk nanocomposites. Interestingly, large increases in the thermopower and large reductions in the thermal conductivity were observed for SS-MA samples with z = 0.01 and 0.03 when compared to SS samples with similar nominal composition. The increase in the thermopower of the MA samples is attributed to a decrease in the effective carrier density due to the filtering of low-energy carriers at the HH/FH interfaces, whereas the reduction in the thermal conductivity is ascribed to effective phonon scattering due to the presence of a high density of grain boundaries and phase boundaries in the SS-MA samples compared to the SS counterpart.

Experimental

Synthesis. The fabrication of bulk semiconducting half-Heusler (HH) alloys with integrated full-Heusler (FH) nanostructures was achieved by reacting high purity (99.99%) Ti, Hf, Sn, and Sb with various concentrations of Ni calculated following the general formula $Ti_{0.4}Hf_{0.6}Ni_{1+z}Sn_{0.975}Sb_{0.025}$ (z = 0.005, 0.01, 0.03). Mixtures of elemental powders in the desired ratio (total mass = 10.0 g) were prepared under Ar atmosphere in a glove box, sealed in a quartz tube under a residual pressure of 10^{-4} Torr, and heated sequentially to 300 °C for 3 days and to 900 °C for 7 days. The resulting products (SS series) were thoroughly mixed using an agate mortar and pestle under an inert Ar-atmosphere and divided into two equal portions. A portion of various SS samples were mechanically alloyed for 2 hr using a high-energy shaker ball mill from SPEX and consolidated into pellets at 950 °C under an applied pressure of 100 MPa using a uniaxial hot press system to produce the SS-MA series of samples. The other portion was consolidated (under similar conditions) into pellets without the ball-milling procedure (SS

samples). Detailed densification procedures are described elsewhere [24, 32-33]. The relative densities of the pressed pellets were obtained by dividing the geometrical density (calculated using the pellet's dimension and mass) by the "true" density of the as-synthesized polycrystalline powder, measured using He gas pycnometry on a Quantachrome Micro Ultrapyc 1200e. The relative density of all hot pressed pellets was above 98%.

Characterization. The constituent phases of the as-prepared and the mechanically alloyed materials were investigated by powder X-ray diffraction using monochromated Cu-*K*α radiation on a rotating anode Rigaku powder diffractometer operating under 40 kV and 40 mA. The transmission electron microscopy (TEM) study of selected specimens cut from pressed pellets was performed with a JEOL-3011 to probe the size and the distribution of FH nanoinclusions embedded within the HH matrix as well as the interface boundary between HH and FH phases. Details on TEM sample preparation are described elsewhere [24, 32-33]. Seebeck coefficient and electrical resistivity were measured simultaneously from room temperature to 500°C under a low pressure He atmosphere using a commercial ZEM-3 system from ULVAC-RIKO. The instrument precision on the electrical resistivity and Seebeck coefficient data is ±4%. The thermal conductivity was calculated from the thermal diffusivity data measured by the laser flash method (LINSEIS; LFA 1000) from 30°C to 500°C under dynamic vacuum (~10^{-3} Torr). The instrument precision on the thermal diffusivity data is ±3%. Pyroceram reference material was measured alongside each sample. The specific heat capacity (*Cp*) used for thermal conductivity ($\kappa = DC_p d$, where d is the geometrical density of the pellet) calculations were extracted from the laser flash data.

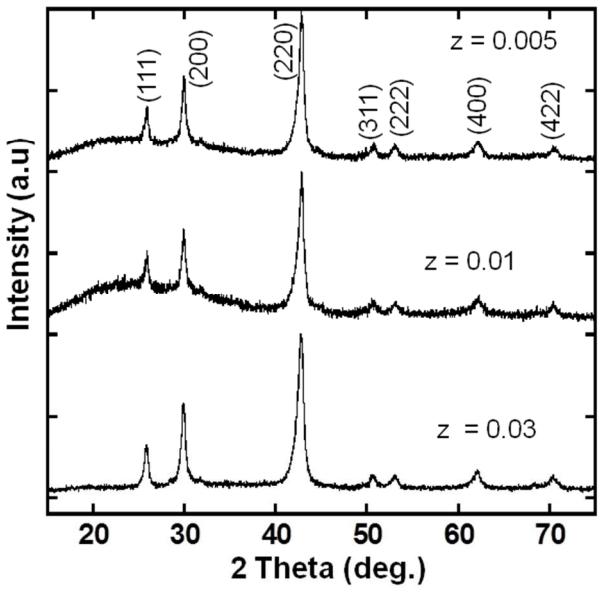

Figure 1: X-ray powder diffraction patterns of $Ti_{0.4}Hf_{0.6}Ni_{1+z}Sb_{0.975}Sn_{0.025}$ ($0.005 \leq z \leq 0.03$) half-Heusler alloys synthesized by solid-state reaction of the elements followed by mechanical alloying using a high energy shaker ball mill.

Results and Discussion

Structural Characterization. The powder X-ray diffraction (XRD) patterns of the synthesized $Ti_{0.4}Hf_{0.6}Ni_{1+z}Sb_{0.975}Sn_{0.025}$ (HH (1-z)/FH(z)) composites are shown in Figure 1. All XRD patterns of the synthesized materials before and after the mechanical alloying steps show only diffraction peaks of the HH matrix (cubic MgAgAs structure-type) suggesting complete reaction of the starting elements. XRD powder patterns of the SS-MA samples showed broad diffraction peaks of the HH phase (Fig. 1) suggesting that the ball milling step provides suitable conditions for the formation nanometer-scale grains of the HH/FH nanocomposites. Surprisingly, no diffraction peaks corresponding to the FH phase anticipated from the chemical equation (1) could be observed in the XRD patterns of the samples before and after mechanical alloying.

$$0.4\ Ti + 0.6\ Hf + (1+z)\ Ni + 0.975\ Sn + 0.025\ Sb \rightarrow (1-z)\ Ti_{0.4}Hf_{0.6}NiSn_{0.975}Sb_{0.025}\ (HH) + z\ Ti_{0.4}Hf_{0.6}Ni_2Sn_{0.975}Sb_{0.025}\ (FH) \quad (1)$$

The absence of the FH peaks on the XRD patterns suggests either the formation of FH precipitates that are too small to strongly diffract X-ray radiation or the dissolution of excess Ni into interstitial sites in the structure of the HH matrix to form interstitial solid-solution. However, the constant value of the unit cell parameters of various $Ti_{0.4}Hf_{0.6}Ni_{1+z}Sb_{0.975}Sn_{0.025}$ HH phases (a ~ 6.050(2) Å) points to the absence of interstitial solid-solution between HH and excess elemental Ni.

To probe the anticipated formation of small precipitates in the synthesized $Ti_{0.4}Hf_{0.6}Ni_{1+z}Sb_{0.975}Sn_{0.025}$ ($0 \leq z \leq 0.03$) samples and also to investigate the effect of the mechanical alloying process on the microstructures of the SS-MA samples, we have performed high resolution transmission electron microscopy (HRTEM) study on selected SS and SS-MA samples. Careful examination of the low magnification (TEM) image of the SS sample with z = 0.03 (HH(97%)/FH(3%)) revealed the presence of small (~20 nm) and larger (~50 nm) precipitates embedded in micron-size grains of the HH matrix (Fig. 2A). The inset of Figure 2(A) shows the low magnification image of a single precipitate with particle size of ~20 nm coherently embedded in the HH matrix. The cubic *fcc* structure of the small precipitates was confirmed by selected area electron diffraction. The observed small and large precipitates are believed to be FH inclusions accordingly with the chemical reaction (1). The formation of FH particles is most likely achieved through spontaneous segregation between the HH and FH

phases in the resulting product, which is driven by the difference in their structure type [23]. TEM images of the sample with z = 0.03 after mechanical alloying (SS-MA-0.03) showed a reduction in the grain size of HH/FH composites from micron-scale grains to small grains with sizes from 5 to 20 nm (Fig. 2B). In this matrix grain size refinement process, large particles of the FH precipitates are also finely divided into 5-8 nm range particles well dispersed between nanometer-scale grains of the HH matrix. In addition to reducing the size of the HH and FH grains, the mechanical allowing step also introduces a thin layer of amorphous phase at the grain boundaries. The cubic *fcc* structures of the mechanical alloyed HH/FH composites was also confirmed by selected area electron diffraction.

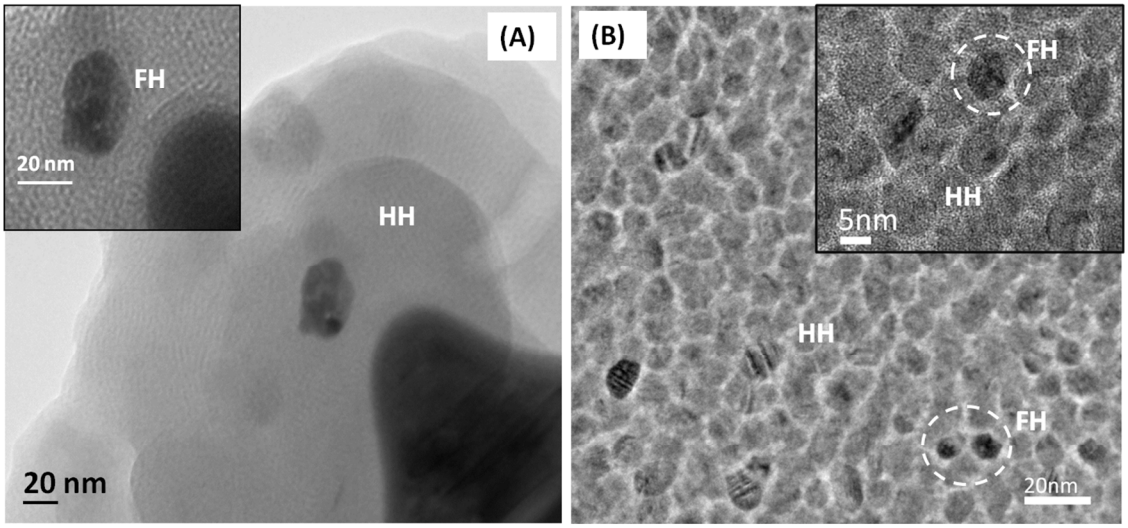

Figure 2: TEM images of $Ti_{0.4}Hf_{0.6}Ni_{1+z}Sb_{0.975}Sn_{0.025}$ half-Heusler alloy with z = 0.03 obtained from solid-state reaction of the elements, before (A) and after (B) mechanical alloying (MA). Before MA, the synthesized composites contain small and large particles of the FH inclusions embedded in micrometer scale grains of the HH matrix. The MA process results in large reduction of the average particle size of the FH inclusions as well as the average grain size of the HH matrix.

The observed reduction in the average size of the FH inclusions down to ~5nm is expected to significantly alter electronic transport within the HH matrix. Our previous work on similar systems showed that nanometer FH inclusions embedded in a HH semiconducting matrix act as energy filter to low-energy electrons at the HH/FH interfaces, leading to large increases in

the thermopower and carrier mobility[23-25]. In addition, the high density of grain boundaries and HH/FH phase boundaries generated in the samples by the mechanical alloying process are anticipated to promote the scattering of a broad range of phonons resulting in large decrease in the thermal conductivity of the SS-MA samples compared to that of the SS samples.

Thermoelectric properties. To assess the effect of the particle size reductions via the MA process on the thermoelectric behavior of various $Ti_{0.4}Hf_{0.6}Ni_{1+z}Sb_{0.975}Sn_{0.025}$ ($0.005 \leq z \leq 0.03$) half-Heusler alloys, we have measured thermal and electronic transport data in the temperature range from 300 K to 775K using pellets of the as-synthesized HH(1-z)/FH(z) composites (SS series) as well as the composites after the MA step (SS-MA series). Figure 3 shows the temperature dependence of the total and lattice thermal conductivities of the HH(1-z)/FH(z) composites before (SS series) and after (SS-MA series) mechanical alloying. $Ti_{0.4}Hf_{0.6}Ni_{1+z}Sb_{0.975}Sn_{0.025}$ samples from solid state reaction (SS) containing various amounts of excess Ni ($0 \leq z \leq 0.03$) show similar values of the thermal conductivity (Fig. 3A). At 300K, the thermal conductivity of the SS-0.005 sample is 8.5 W/m·K and monotonically decreases with rising temperature reaching a value of ~6.5 W/m·K at 775K. A similar trend was observed for the temperature dependent thermal conductivity of SS samples with z = 0.01 and 0.03. The observed total thermal conductivities of the SS samples are comparable to values measured in HH phases with similar compositions [27, 34]. Regardless of the temperature, the thermal conductivities of SS samples slightly increase with increasing excess of Ni (increasing FH content). Interestingly, drastic reductions in the total thermal conductivity are observed for SS samples with z = 0.005, 0.01 and 0.03 after grain size reduction through the high energy ball milling process. For example, the thermal conductivity of the SS-MA-0.005 sample is ~ 4.9 W/m·K at 300 K (Fig 3B). This corresponds to a 42% reduction when compared to the thermal conductivity of SS-0.005 sample (Fig. 3A). The largest reduction in the thermal conductivity is observed for the SS-MA sample with z = 0.03, which contains the highest density of HH/FH phases boundaries. The thermal conductivity value at 300K is ~ 4.0 W/m·K, which is ~ 55% lower than the value of 8.9 W/m·K measured at the same temperature for the SS sample with similar nominal composition. The thermal conductivities of all mechanically alloyed samples marginally change with increasing temperature. The observed large decrease in the total thermal conductivity of $Ti_{0.4}Hf_{0.6}Ni_{1+z}Sb_{0.975}Sn_{0.025}$ samples after mechanical alloying is attributed to the

scattering charge carriers and a wide range of phonons at multiple grains boundaries and HH/FH phase boundaries in the samples. Charge carriers scattering at grain and phase boundaries result in a reduction of carrier mobility leading to a decrease electronic contribution to the total thermal conductivity, whereas efficient phonon scattering at multiple grain and phase boundaries results in a reduction in the lattice thermal conductivity.

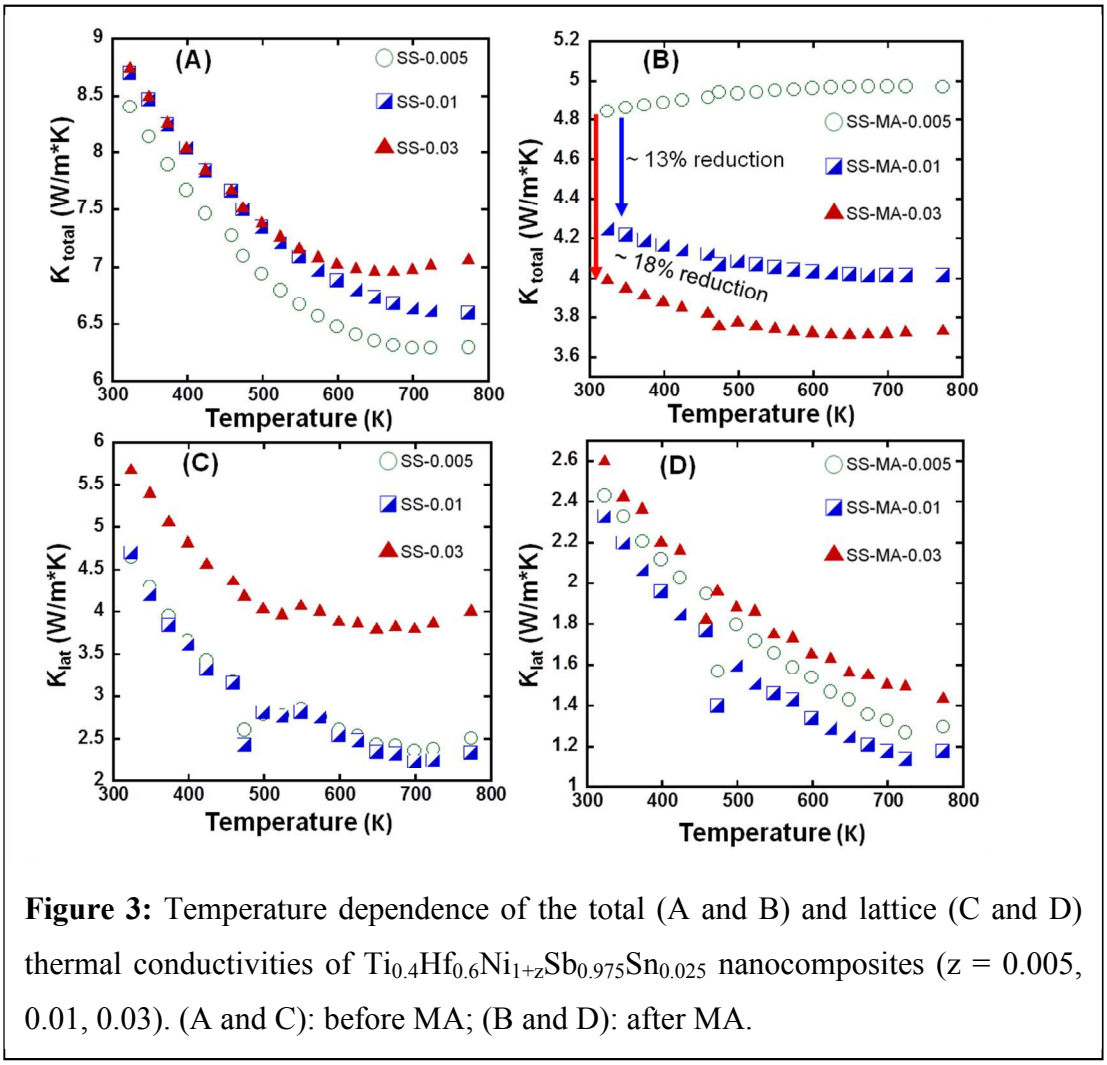

Figure 3: Temperature dependence of the total (A and B) and lattice (C and D) thermal conductivities of $Ti_{0.4}Hf_{0.6}Ni_{1+z}Sb_{0.975}Sn_{0.025}$ nanocomposites (z = 0.005, 0.01, 0.03). (A and C): before MA; (B and D): after MA.

Figures 3C and 3D show the temperature dependence of the lattice thermal conductivity of the as-synthesized $Ti_{0.4}Hf_{0.6}Ni_{1+z}Sb_{0.975}Sn_{0.025}$ samples and the mechanical alloyed samples, respectively. The lattice thermal conductivity (κ_L) was obtained by subtracting the electronic component κ_e from the total thermal conductivity, κ. κ_e was estimated using the Wiedemann-Franz law, $\kappa_e = L_o \sigma T$, where $L_o = 2.45 \times 10^{-8}$ $W\Omega K^{-2}$ is the Lorentz number. At 300 K, the lattice

thermal conductivity of the SS-0.005 sample is ~4.6 W/m·K and decreases with rising temperature to ~2.5 W/m·K at 775 K (Fig. 3C). Similar values of the lattice thermal conductivities were observed for $Ti_{0.4}Hf_{0.6}Ni_{1+z}Sb_{0.975}Sn_{0.025}$ samples with z = 0.01. Increasing the Ni content to z = 0.03 resulted in a 28% increase of the lattice thermal conductivity to ~5.9 W/m·K at 300 K. The observed increase in the lattice thermal conductivity of the SS-0.03 sample suggests that at this level of excess Ni, FH particles are sufficiently large to contribute to both the thermal and electronic transport properties of the HH(1-z)/FH(z) composites. After mechanical alloying using high-energy shaker milling, the lattice thermal conductivity of all samples drastically decrease. At 300 K, the lattice thermal conductivities vary from 2.4 W/m·K for the sample with z = 0.01 to 2.6 W/m·K for the sample with z = 0.03. These values correspond to ~ 50% decrease when compared to the thermal conductivity of the as-synthesized $Ti_{0.4}Hf_{0.6}Ni_{1+z}Sb_{0.975}Sn_{0.025}$ samples. Remarkably, the thermal conductivity of mechanically alloyed samples further decrease with rising temperature reaching values as low as 1.2 W/m·K at 775 K for the sample with z = 0.01. The observed values of the lattice thermal conductivity of mechanically alloyed $Ti_{0.4}Hf_{0.6}Ni_{1+z}Sb_{0.975}Sn_{0.025}$ HH(1-z)/FH(z) nanocomposites is among the lowest lattice thermal conductivities reported for HH samples[27, 35-36]. The low lattice thermal conductivities of $Ti_{0.4}Hf_{0.6}Ni_{1+z}Sb_{0.975}Sn_{0.025}$ HH(1-z)/FH(z) nanocomposites resulted from the scattering of a broad range of phonon by the high density nanometer-scale grains boundaries and HH/FH phase boundaries generated by the mechanical alloying process.

The temperature dependence of the electrical conductivity and thermopower of the as-synthesized $Ti_{0.4}Hf_{0.6}Ni_{1+z}Sb_{0.975}Sn_{0.025}$ nanocomposites and the mechanically alloyed counterparts are shown in Figure 4. The electrical conductivity of the SS-0.005 sample is ~ 4750 S/cm at 300K and decreases with increasing temperature reaching a value of ~2000 S/cm at 775 K. This temperature dependence of the electrical conductivity of the SS-0.005 sample is consistent with heavily doped semiconducting behavior. Interestingly, all SS samples regardless of the fraction of FH inclusions (z values) show similar values of electrical conductivity in the whole temperature range (Fig. 4A). The temperature dependence of the thermopower of the as-synthesized $Ti_{0.4}Hf_{0.6}Ni_{1+z}Sb_{0.975}Sn_{0.025}$ nanocomposites is shown in Figure 4C. All samples show negative values of the thermopower in the whole temperature range indicating n-type semiconducting behavior. At 300K, the thermopower of the sample with z = 0.005 (SS-0.005) is ~ -60 μV/K and increases almost linearly with rising temperature reaching a value of -120 μV/K

at 775K. Regardless of the z values, similar values of the thermopower as well as its temperature dependence were observed for the as-synthesized $Ti_{0.4}Hf_{0.6}Ni_{1+z}Sb_{0.975}Sn_{0.025}$ nanocomposites. The observed comparable values of the electrical conductivities and thermopower at all temperatures for the as-synthesized $Ti_{0.4}Hf_{0.6}Ni_{1+z}Sb_{0.975}Sn_{0.025}$ nanocomposites suggest that the embedded FH nanoinclusions are not electronically active (i.e. they do not contribute additional carriers to the HH matrix) and are transparent to carrier flow. However, this electronic behavior drastically changes when the as-synthesized $Ti_{0.4}Hf_{0.6}Ni_{1+z}Sb_{0.975}Sn_{0.025}$ nanocomposites are subjected to mechanical alloying using high energy shaker ball mill. In general, all mechanical alloyed samples showed lower electrical conductivity at all temperatures when compared to the values observed for the as-synthesized HH(1-z)/FH(z) nanocomposites with similar composition (Fig. 4B).

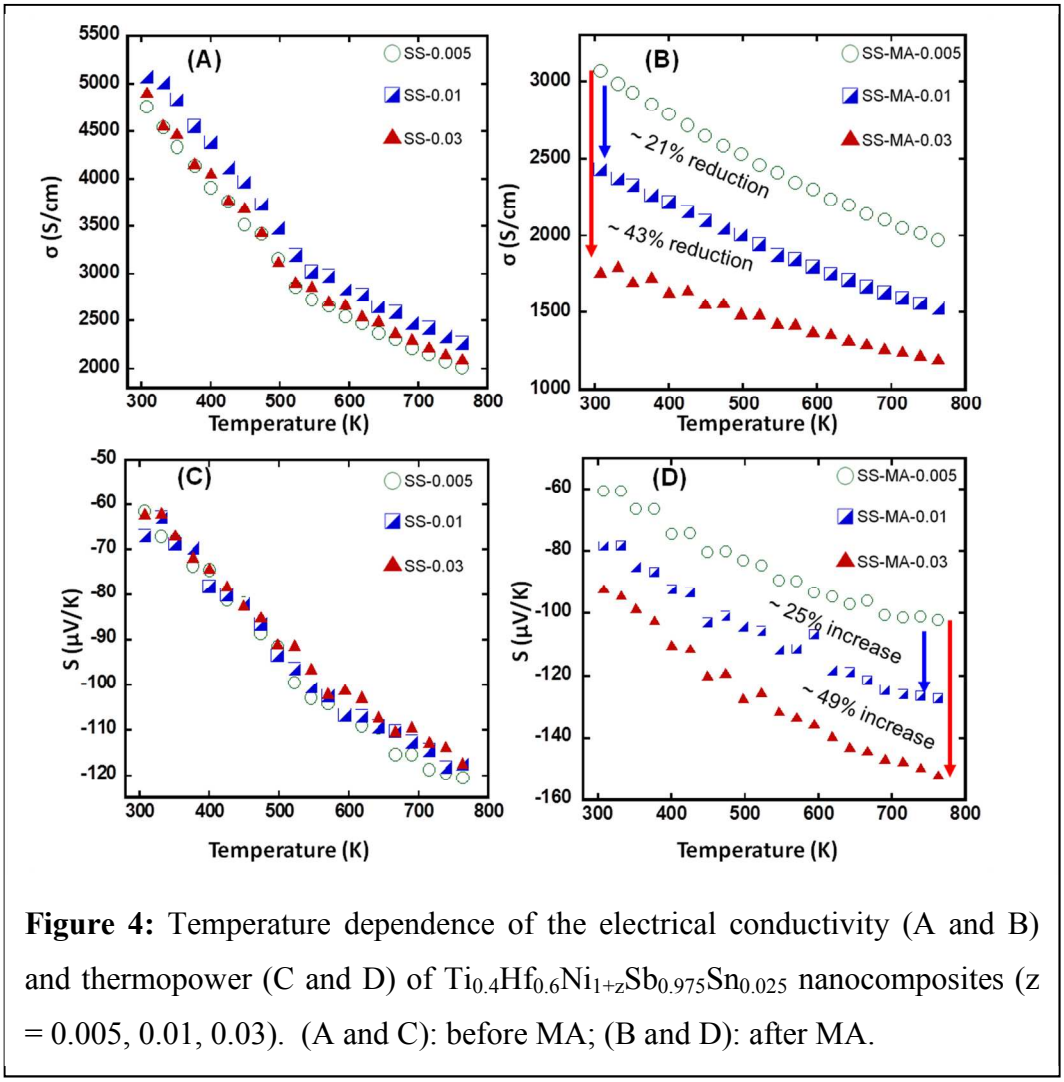

Figure 4: Temperature dependence of the electrical conductivity (A and B) and thermopower (C and D) of $Ti_{0.4}Hf_{0.6}Ni_{1+z}Sb_{0.975}Sn_{0.025}$ nanocomposites (z = 0.005, 0.01, 0.03). (A and C): before MA; (B and D): after MA.

However, the magnitude of the drop in the electrical conductivity depends on the mole fraction of FH inclusions (z value) in the sample. Likewise, larger values of the thermopower are observed for the mechanically alloyed samples (z = 0.01 and 0.03) when compared to the value obtained for the as-synthesized nanocomposites with similar composition (Fig. 4D). The magnitude of the increase in the thermopower varies with the mole fraction of FH inclusions in the sample.

To fully understand the nature of the observed variations in the electronic transport properties of $Ti_{0.4}Hf_{0.6}Ni_{1+z}Sb_{0.975}Sn_{0.025}$ nanocomposites after mechanical alloying, we have carefully examined the changes in the electrical conductivity and thermopower of each composition (before and after MA) within the context of the effect of matrix grain boundaries and matrix/inclusion phase boundaries on the alteration of carrier density and/or carrier mobility within the samples. Figure 4B shows the temperature dependence of the electrical conductivity of all SS-MA samples. At 300K, the electrical conductivity of the sample with z = 0.005 (SS-MA-0.005) is ~ 3000 S/cm, which corresponds to a 37% decrease when compared to the electrical conductivity of the SS-0.005 sample at the same temperature. Interestingly, the electrical conductivity slowly decreases with rising temperature reaching a value of ~ 2000 S/cm at 775 K, which is similar to the electrical conductivity observed for the as-synthesized SS-0.005 nanocomposites at the same temperature. Despite the large decrease in the electrical conductivity of SS-MA-0.005 sample at 300 K, the thermopower remains unchanged (~-60 μV/K) indicating that the observed drop in the electrical conductivity results from a large reduction in the carrier mobility due to the high density grain boundaries introduced by the mechanical alloying process. The thermopower of the SS-MA-0.005 sample increases with rising temperature reaching -102 μV/K at 775 K (Fig. 4D). This value is 15% smaller than that of the SS-0.005 sample at the same temperature, suggesting a marginal increase in the carrier density of the MA samples through thermal activation at high temperatures. It is remarkable to note that unlike the as-synthesized $Ti_{0.4}Hf_{0.6}Ni_{1+z}Sb_{0.975}Sn_{0.025}$ nanocomposites, which showed similar values of the electrical conductivity and thermopower at all temperatures regardless of the fraction of FH inclusions (z value), a drastic alteration of the electrical conductivity and thermopower with increasing mole fractions of FH inclusions is observed for the mechanically alloyed samples. For instance, the room temperature values of the electrical conductivity decrease to 2500 S/cm for the SS-MA-0.01 sample (z = 0.01) and to 1750 S/cm for the SS-MA-0.03 sample (z = 0.03). The electrical

conductivity of both samples slowly decrease with increasing temperature reaching 1500 S/cm (SS-MA-0.01) and 1200 S/cm (SS-MA-0.03) at 775 K (Fig. 4B). The observed room temperature values of the electrical conductivities for the SS-MA-0.01 and SS-MA-0.03 samples are respectively 47% and 63% lower than the electrical conductivity of the as-synthesized nanocomposites with similar nominal compositions. Several factors contribute to this sharp drop in electrical conductivity. The primary contributor is the reduction in carrier mobility due to the scattering of charge carriers at multiple grains boundaries introduced through the mechanical alloying process. As observed for the SS-MA-0.005 sample, reduction in the electrical conductivity due to grain boundaries amount to ~37%. Therefore, additional reductions in the electrical conductivity observed for the SS-MA-0.01 and SS-MA-0.03 samples presumably result from the decrease in the effective density of charge carriers in the samples. Our previous work in similar HH/FH composites [24-25] showed that the formation of coherent nanometer scale (<10 nm) FH inclusions into a semiconducting HH matrix lead to a sharp drop in the effective carrier density in the resulting nanocomposites. Such reduction in the effective carrier density was attributed to the filtering of low-energy carriers by the potential energy barrier resulting from the offset of the conduction band minima (CBM) at the HH/FH interfaces. The mechanical alloying processing of the synthesized $Ti_{0.4}Hf_{0.6}Ni_{1+z}Sb_{0.975}Sn_{0.025}$ nanocomposites favors the formation of such nanometer scale HH/FH interfaces in the SS-MA samples, the density of which increases with increasing FH content (z value). Therefore, it can be speculated that the observed additional reductions in the electrical conductivities of the SS-MA-0.01 and SS-MA-0.03 samples result from the reduction in the effective carrier density. Within this picture, one should expect some increase in the thermopower of SS-MA-0.01 and SS-MA-0.03 samples. Indeed, the room temperature values of the thermopower of SS-MA-0.01 and SS-MA-0.03 samples are -78 μV/K and -92 μV/K, respectively (Fig 4D). These values correspond to 30% (SS-MA-0.01) and 53% (SS-MA-0.03) increase in the thermopower when compared to SS samples with similar composition. The thermopower of the SS-MA-0.01 and SS-MA-0.03 samples increase with rising temperatures reaching -128 μV/K (SS-MA-0.01) and -152 μV/K (SS-MA-0.03) at 775 K.

The temperature dependence of the power factor (PF) of the as-synthesized $Ti_{0.4}Hf_{0.6}Ni_{1+z}Sb_{0.975}Sn_{0.025}$ nanocomposites is shown in Figure 5A. At 300 K, the PF of the SS-0.005 sample is 1800 $\mu W/K^2m$ and gradually increases with temperature reaching a maximum of 3000 $\mu W/K^2m$ at 700 K. The PF of the SS-0.03 sample are comparable to those of the SS-0.005

sample at all temperatures, which is consistent with the observed similarity in the electrical conductivity and thermopower of various $Ti_{0.4}Hf_{0.6}Ni_{1+z}Sb_{0.975}Sn_{0.025}$ nanocomposites. The SS-0.01 sample displays a slightly higher PF (2300 μW/K^{2}m at 300K and 3250 μW/K^{2}m at 775 K) when compared to the SS-0.005 sample. The observed marginal increase in the PF of SS-0.01 sample is consistent with its slightly higher electrical conductivity and thermopower when compared to other $Ti_{0.4}Hf_{0.6}Ni_{1+z}Sb_{0.975}Sn_{0.025}$ nanocomposites. After the mechanical alloying process, SS-MA samples with z = 0.005 and 0.01 show lower PF compared to SS samples with similar composition (Fig. 5B), whereas the PF of the SS-MA-0.03 sample remains fairly constant. However, the magnitude of the drop in the PF varies with the mole fraction of FH inclusions (z value). The observed drop in the PF of SS-MA-0.005 (1000 μW/K^{2}m at 300 K), SS-MA-0.01 (1500 μW/K^{2}m at 300 K) is consistent with the large reduction in the electrical conductivity (Fig. 4B). For the SS-MA-0.03 sample, the drop in the electrical conductivity is partially compensated by an increase in the thermopower leading to marginal drop in the PF (1500 μW/K^{2}m at 300 K and 2800 μW/K^{2}m at 775 K).

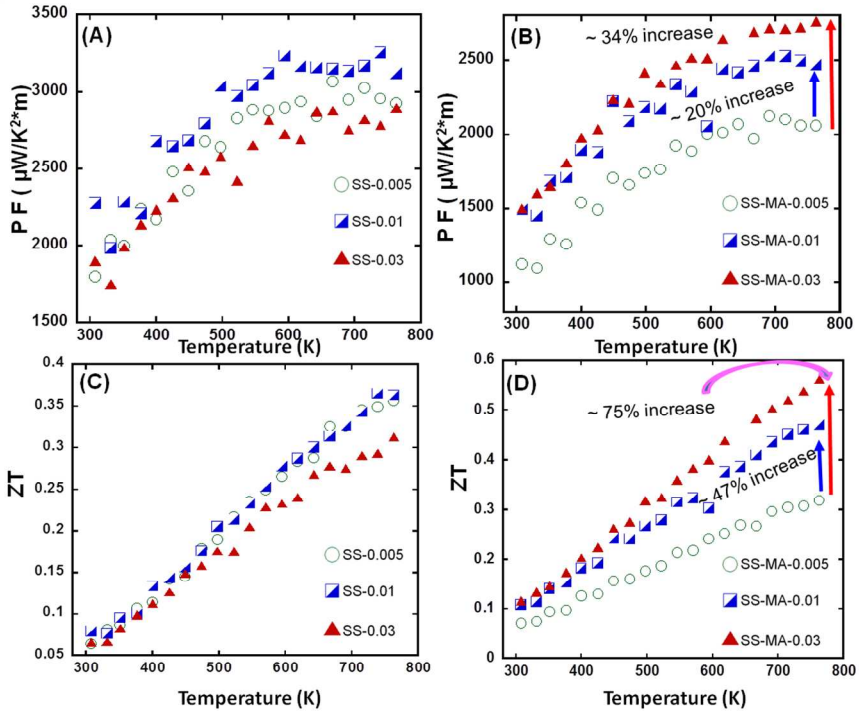

Figure 5: Temperature dependence of the Power Factor (A and B) and Figure of Merit (C and D) of $Ti_{0.4}Hf_{0.6}Ni_{1+z}Sb_{0.975}Sn_{0.025}$ nanocomposites (z = 0.005, 0.01, 0.03) before (A and C) and after (B and D) mechanical alloying.

Figure 5C shows the temperature dependence of the thermoelectric figure of merit (ZT) for the as-synthesized $Ti_{0.4}Hf_{0.6}Ni_{1+z}Sb_{0.975}Sn_{0.025}$ nanocomposites. At 300 K, the SS-0.005 sample shows a ZT~0.06, which linearly increases with rising temperature reaching a value of ~0.36 at 775 K. Comparable ZT values were observed at all temperature range for all SS samples. After the mechanical alloying process, large ZT improvements were observed for SS-MA-0.01 and SS-MA-0.03 samples, when compared to the ZT obtained from SS samples with similar compositions. At 300 K, both samples showed ZT value of ~ 0.12, which rapidly increases with temperature reaching ZT~ 0.5 (for SS-MA-0.01) and ZT ~ 0.6 (for SS-MA-0.03) at 775 K. The observed ZT values for SS-MA-0.01 and SS-MA-0.03 at 775 K correspond to 31% (SS-MA-0.01) and 81% (SS-MA-0.03) enhancements when compared to the ZT value of the as-synthesized $Ti_{0.4}Hf_{0.6}Ni_{1+z}Sb_{0.975}Sn_{0.025}$ nanocomposites with similar composition. The observed improvements in the figures of merit of SS-MA-0.01 and SS-MA-0.03 samples result from (1) large decrease in their total thermal conductivity arising from the effective scattering of a broad range of the phonon spectrum by nanometer-scale grain boundaries and HH/FH phase boundaries and (2) marginal decrease in the PF due to large increase in the thermopower arising from the filtering of a significant fraction of low-energy carrier at nanometer-scale HH/FH interfaces.

Conclusions

In summary, we have investigated the effect of grain boundary and phase boundary engineering via mechanical alloying on the thermal and electronic transports in nanostructured n–type $Ti_{0.4}Hf_{0.6}Ni_{1+z}Sb_{0.975}Sn_{0.025}$ **(**HH(1-z)/FH(z)) bulk composites synthesized by high temperature solid-state reaction of the elements. We found that FH nanoinclusions coherently embedded in bulk heavily-doped HH matrices have marginal effect on the overall electronic and thermal transport of the resulting composites. However, reducing the particles size of the bulk HH/FH composites to the nanometer range (<20 nm) by mechanical alloying using high energy shaker ball milling led to drastic alterations of thermal and electronic transport in the resulting nanocomposites. Large reductions (up 55% for SS-MA-0.03) in the total and lattice thermal conductivities were observed on SS-MA samples containing various fractions of FH inclusions. Thermal conductivity values as low as 3.8 W/m·K, were observed at 775 K for the SS-MA-0.03 sample. The observed reduction in the thermal conductivity is attributed to the scattering of a

broad range of phonons at multiple grain boundaries and matrix-inclusions phase boundaries generated by the mechanical alloying process. Interestingly, in the process of reducing the particles of the synthesized polycrystalline powders of bulk HH(1-z)/FH(z) composites, FH inclusions embedded in various particles within the HH matrix are also broken down into smaller (< 5 nm) precipitates. This leads to the creation of high density, well dispersed nanometer-scale HH/FH interfaces in the resulting HH(1-z)/FH(z) nanocomposites. Such nanometer-scale coherent HH/FH interfaces are believed to act as filters to low-energy electrons leading to large increases in the thermopower of SS-MA-0.01 and SS-MA-0.03 samples. This offsets the drop in the electrical conductivity arising from enhanced electron scattering at grain boundaries mitigating the reduction of the power factor. Therefore, large improvements (up to 81%) are observed in the figures of merit of $Ti_{0.4}Hf_{0.6}Ni_{1+z}Sb_{0.975}Sn_{0.025}$ bulk composites after mechanical alloying. This work demonstrates that one can efficiently reduce the thermal conductivity of heavily doped HH semiconductors with marginal alteration of the PF through the formation of well dispersed nanometer-scale coherent FH nanostructures and generation of nanometer-scale grain boundaries using mechanical alloying. The implementation of this simple strategy on fully optimized HH matrices is expected to further increase their thermoelectric figure of merit.

Acknowledgements

P.F.P.P. gratefully acknowledges financial support from the Department of Energy, Office of Basic Energy Sciences under Award # DE-SC-0008574. This work made use of the TEM from the University of Michigan's Electron Microbeam Analysis Laboratory (EMAL), purchased with funds from the National Science Foundation Awards DMR-0315633 and DMR-0723032.

References

1 Y. Cao, X. Zhao, T. Zhu, X. Zhang, J. Tu, Syntheses and thermoelectric properties of BiTe/SbTe bulk nanocomposites with laminated nanostructure, *Applied Physics Letters*, 2008, **92**, 143106.

2 B. Poudel, Q. Hao, Y. Ma, Y. Lan, A. Minnich, B. Yu, X. Yan, D. Wang, A. Muto, D. Vashaee, High-thermoelectric performance of nanostructured bismuth antimony telluride bulk alloys, *Science*, 2008, **320**, 634.

3 H. Li, X. Tang, Q. Zhang, C. Uher, High performance InCeCoSb thermoelectric materials with in situ forming nanostructured InSb phase, *Applied Physics Letters*, 2009, **94**, 102114.

4 M. Ibáñez, D. Cadavid, R. Zamani, N. García-Castelló, V. Izquierdo-Roca, W. Li, A. Fairbrother, J. D. Prades, A. Shavel, J. Arbiol, Composition control and thermoelectric

properties of quaternary chalcogenide nanocrystals: the case of stannite $Cu_2CdSnSe_4$, *Chemistry of Materials*, 2012, **24**, 562.
5 M. G. Kanatzidis, Nanostructured Thermoelectrics: The New Paradigm?, *Chemistry of Materials*, 2010, **22**, 648.
6 A. J. Minnich, M. S. Dresselhaus, Z. F. Ren, G. Chen, Bulk nanostructured thermoelectric materials: current research and future prospects, *Energy & Environmental Science*, 2009, **2**, 466.
7 M. S. Dresselhaus, G. Chen, M. Y. Tang, R. Yang, H. Lee, D. Wang, Z. Ren, J. P. Fleurial, P. Gogna, New Directions for Low-Dimensional Thermoelectric Materials, *Advanced Materials*, 2007, **19**, 1043.
8 L. D. Hicks, M. S. Dresselhaus, Thermoelectric Figure of Merit of a One-Dimensional Conductor, *Physical Review B*, 1993, **47**, 16631.
9 W. Kim, J. Zide, A. Gossard, D. Klenov, S. Stemmer, A. Shakouri, A. Majumdar, Thermal conductivity reduction and thermoelectric figure of merit increase by embedding nanoparticles in crystalline semiconductors, *Physical Review Letters*, 2006, **96**, 045901.
10 N. Sato, Y. Matsuura, K. Kitahara, Y. Takagiwa, K. Kimura, Thermoelectric figure of merit enhancement of intermetallic compound $RuGa_2$ by ball-milling, *Journal of Alloys and Compounds*, 2014, **585**, 455.
11 H. Alam, S. Ramakrishna, A review on the enhancement of figure of merit from bulk to nano-thermoelectric materials, *Nano Energy*, 2013, **2**, 190.
12 T. Harman, P. Taylor, D. Spears, M. Walsh, Thermoelectric quantum-dot superlattices with high ZT, *Journal of Electronic Materials*, 2000, **29**, L1.
13 D. Broido, T. Reinecke, Theory of thermoelectric power factor in quantum well and quantum wire superlattices, *Physical Review B*, 2001, **64**, 045324.
14 P. F. P. Poudeu, J. D'Angelo, A. D. Downey, J. L. Short, T. P. Hogan, M. G. Kanatzidis, High thermoelectric figure of merit and nanostructuring in bulk p-type $Na_{1-x}Pb_mSb_yTe_{m+2}$, *Angewandte Chemie-International Edition*, 2006, **45**, 3835.
15 R. Venkatasubramanian, E. Siivola, T. Colpitts, B. O'Quinn, Thin-film thermoelectric devices with high room-temperature figures of merit, *Nature*, 2001, **413**, 597.
16 A. I. Hochbaum, R. K. Chen, R. D. Delgado, W. J. Liang, E. C. Garnett, M. Najarian, A. Majumdar, P. D. Yang, Enhanced thermoelectric performance of rough silicon nanowires, *Nature*, 2008, **451**, 163.
17 A. I. Boukai, Y. Bunimovich, J. Tahir-Kheli, J. K. Yu, W. A. Goddard, J. R. Heath, Silicon nanowires as efficient thermoelectric materials, *Nature*, 2008, **451**, 168.
18 Y.-M. Lin, M. Dresselhaus, Thermoelectric properties of superlattice nanowires, *Physical Review B*, 2003, **68**, 075304.
19 J. Heremans, C. M. Thrush, Y.-M. Lin, S. Cronin, Z. Zhang, M. Dresselhaus, J. Mansfield, Bismuth nanowire arrays: Synthesis and galvanomagnetic properties, *Physical Review B*, 2000, **61**, 2921.
20 J. Zhou, X. Li, G. Chen, R. Yang, Semiclassical model for thermoelectric transport in nanocomposites, *Physical Review B*, 2010, **82**, 115308.
21 J. Martin, L. Wang, L. Chen, G. Nolas, Enhanced Seebeck coefficient through energy-barrier scattering in PbTe nanocomposites, *Physical Review B*, 2009, **79**, 115311.
22 A. Popescu, L. M. Woods, J. Martin, G. S. Nolas, Model of transport properties of thermoelectric nanocomposite materials, *Physical Review B*, 2009, **79**, 205302.

23 P. Sahoo, Y. F. Liu, J. P. A. Makongo, X. L. Su, S. J. Kim, N. Takas, H. Chi, C. Uher, X. Q. Pan, P. F. P. Poudeu, Enhancing thermopower and hole mobility in bulk p-type half-Heuslers using full-Heusler nanostructures, *Nanoscale*, 2013, **5**, 9419.

24 J. P. A. Makongo, D. K. Misra, X. Y. Zhou, A. Pant, M. R. Shabetai, X. L. Su, C. Uher, K. L. Stokes, P. F. P. Poudeu, Simultaneous Large Enhancements in Thermopower and Electrical Conductivity of Bulk Nanostructured Half-Heusler Alloys, *Journal of the American Chemical Society*, 2011, **133**, 18843.

25 Y. F. Liu, P. Sahoo, J. P. A. Makongo, X. Y. Zhou, S. J. Kim, H. Chi, C. Uher, X. Q. Pan, P. F. P. Poudeu, Large Enhancements of Thermopower and Carrier Mobility in Quantum Dot Engineered Bulk Semiconductors, *Journal of the American Chemical Society*, 2013, **135**, 7486.

26 Y. Liu, A. Page, P. Sahoo, H. Chi, C. Uher, P. F. P. Poudeu, Electronic and Phonon Transports in Sb-doped $Ti_{0.1}Zr_{0.9}Ni_{1+x}Sn_{0.975}Sb_{0.025}$ Nanocomposites *Dalton Transactions*, 2014, **43**, DOI: 10.1039/C4DT00430B.

27 H. Hohl, A. P. Ramirez, C. Goldmann, G. Ernst, B. Wolfing, E. Bucher, Efficient dopants for ZrNiSn-based thermoelectric materials, *Journal of Physics-Condensed Matter*, 1999, **11**, 1697.

28 J. E. Douglas, C. S. Birkel, N. Verma, V. M. Miller, M.-S. Miao, G. D. Stucky, T. M. Pollock, R. Seshadri, Phase stability and property evolution of biphasic Ti–Ni–Sn alloys for use in thermoelectric applications, *Journal of Applied Physics*, 2014, **115**, 043720.

29 C. S. Birkel, J. E. Douglas, B. R. Lettiere, G. Seward, Y. Zhang, T. M. Pollock, R. Seshadri, G. D. Stucky, Influence of Ni nanoparticle addition and spark plasma sintering on the TiNiSn–Ni system: Structure, microstructure, and thermoelectric properties, *Solid State Sciences*, 2013, **26**, 16.

30 P. K. Huang, J. W. Yeh, T. T. Shun, S. K. Chen, Multi-principal-element alloys with improved oxidation and wear resistance for thermal spray coating, *Advanced Engineering Materials*, 2004, **6**, 74.

31 X. F. Wang, Y. Zhang, Y. Qiao, G. L. Chen, Novel microstructure and properties of multicomponent $CoCrCuFeNiTi_x$ alloys, *Intermetallics*, 2007, **15**, 357.

32 J. P. A. Makongo, D. K. Misra, J. R. Salvador, N. J. Takas, G. Y. Wang, M. R. Shabetai, A. Pant, P. Paudel, C. Uher, K. L. Stokes, P. F. P. Poudeu, Thermal and electronic charge transport in bulk nanostructured $Zr_{0.25}Hf_{0.75}NiSn$ composites with full-Heusler inclusions, *Journal of Solid State Chemistry*, 2011, **184**, 2948.

33 D. K. Misra, J. P. A. Makongo, P. Sahoo, M. R. Shabetai, P. Paudel, K. L. Stokes, P. F. P. Poudeu, Microstructure and Thermoelectric Properties of Mechanically Alloyed $Zr_{0.5}Hf_{0.5}Ni_{0.8}Pd_{0.2}Sn_{0.99}Sb_{0.01}/WO_3$ Half-Heusler Composites, *Science of Advanced Materials*, 2011, **3**, 607.

34 S. Sakurada, N. Shutoh, Effect of Ti substitution on the thermoelectric properties of (Zr, Hf) NiSn half-Heusler compounds, *Applied Physics Letters*, 2005, **86**, 082105.

35 Q. Shen, L. Chen, T. Goto, T. Hirai, J. Yang, G. Meisner, C. Uher, Effects of partial substitution of Ni by Pd on the thermoelectric properties of ZrNiSn-based half-Heusler compounds, *Applied Physics Letters*, 2001, **79**, 4165.

36 R. Downie, D. MacLaren, J.-W. Bos, Thermoelectric performance of multiphase XNiSn (X= Ti, Zr, Hf) half-Heusler alloys, *Journal of Materials Chemistry A*, 2014.

Table of Contents Synopsis

The generation of nanometer-scale interfaces in $Ti_{0.4}Hf_{0.6}Ni_{1+z}Sb_{0.975}Sn_{0.025}$ composites induces significant reduction in the thermal conductivity leading to improved ZT.